RESEARCH ARTICLE

Large Area Growth and Phase Selectivity of MoTe₂ Nanosheets through Simulation-Guided CVD Tellurization

Pinaka Pani Tummala, Sara Ghomi, Carlo Spartaco Casari, Christian Martella, Alessio Lamperti,* and Alessandro Molle

Among transition metal dichalcogenides, molybdenum ditelluride (MoTe₂) holds significant attention due to its polymorphic nature including semiconducting, metallic, and topological semimetal phases. Considerable efforts are devoted to synthesizing MoTe₂ nanosheets to make them suitable for device integration in nanotechnologies and for fundamental investigations. In this respect, chemical vapor deposition (CVD) via tellurization of a pre-deposited Mo thin film is an easy and flexible way for synthesizing large scale MoTe₂ nanosheets. Here, the study report on the CVD of large-area (up to 4 cm × 1 cm) MoTe₂ nanosheets with pure 1T' and 2H phase selection by design. Within the tellurization scheme, the vapor-solid reaction between the pre-deposited molybdenum film and tellurium vapor is studied thus optimizing the scalability and quality of the MoTe₂ nanosheets grown on SiO₂/Si substrates. It is demonstrated that the MoTe₂ structure and morphology are kinetically dictated by the tellurium concentration gradient on the reaction site with varying geometric configurations inside the CVD reactor. This study provides a pivot scheme for enabling scalable 1T' and 2H-MoTe₂ integration in applications for novel micro- and nano-electronics, spintronics, photonics, and thermoelectric devices.

P. P. Tummala, S. Ghomi, C. Martella, A. Lamperti, A. Molle
CNR IMM
Unit of Agrate Brianza
via C. Olivetti 2, Agrate Brianza 20864, Italy
E-mail: alessio.lamperti@mdm.imm.cnr.it
P. P. Tummala
Dipartimento di Matematica e Fisica
Università Cattolica del Sacro Cuore
via della Garzetta 48, Brescia 25133, Italy
P. P. Tummala
Department of Physics and Astronomy
KU Leuven
Celestijnenlaan 200D, Leuven 3001, Belgium
S. Ghomi, C. S. Casari
Dipartimento di Energia
Politecnico di Milano
via Ponzio 34/3, Milano 20133, Italy

The ORCID identification number(s) for the author(s) of this article can be found under https://doi.org/10.1002/admi.202200971.

1. Introduction

Among the 2D materials, transition metal dichalcogenides (TMDs) have received much attention for their remarkable properties.[1,2] TMDs have the chemical formula MX₂, where M is a transition metal atom (e.g., Mo, W) and X refers to a chalcogen atom (e.g. S, Se, Te).[2,3] Compared to other TMDs, molybdenum ditelluride (MoTe₂) recently received an intense research interest due to its process tunable allotropic phases, namely the metallic 1T' and the semiconducting 2H phase.[4,5] The 1T' phase, showing orthorhombic structure, is also the precursor stage to access outstanding topological properties and assumes peculiar interests at single and multilayer level as host for the quantum spin hall effect and for the type-II Weyl semi-metallic state that arises in the monoclinic T_d phase as low-temperature distortion of the pristine 1T' phase.[6,7] As the thickness decreases, MoTe₂ exhibits indirect-to-direct bandgap transition while its bandgap is relatively lower than in other TMDs[8,9] ranging from 0.8 eV in case of bulk to 1.1 eV in the monolayer limit.[10] Furthermore, as the electrical conductivity of 1T'-MoTe₂ is much higher than that of the 2H phase, the 1T' phase is promising for solid-state battery electrodes, electrochemical capacitors and hydrogen evolution reaction.[11] On the other hand, 2H-MoTe₂ holds potential as 2D layered material in nanotechnologies due to its small bandgap, strong adsorption, and low thermal conductivity.[10,12] Due to slight energy differences between the two admitted allotropic phases, MoTe₂ represents a unique model material for studying the phase change properties with many related applications such as 2D non-volatile memory devices and memristors in the field of microelectronics.[13,14] Moreover, 2H-MoTe₂ is also a suitable candidate for applications such as field-effect transistors, optoelectronics, energy storage, chemical and biological sensing because of its high carrier mobility, optical transparency, thin structure and chemical stability.[15,16] As a promising material for various applications, a clear understanding and reproducible growth approach is critically important to lift MoTe₂ from lab to production level.

Traditionally, few-layer TMDs such as MoS₂, WS₂, and MoTe₂ can be obtained using mechanical exfoliation, physical

ADVANCED
SCIENCE NEWS
www.advancedsciencenews.com

ADVANCED
MATERIALS
INTERFACES
www.advmatinterfaces.de

vapor deposition and chemical exfoliation, that are limited to a research scope due to their imprecise phase control, uncontrollable coverage, thickness, and non-uniformity.[17–19] Therefore, a precise knowledge of the dynamic phase transition and the growth variables for the large-area, few-layer $MoTe_2$ nanosheets is essential for its integration in various potential applications in different fields.[4,20] Despite the relatively low energy formation difference (40 meV per formula unit) between the 1T' and 2H phase, few studies in literature reported that the phase transition in chemical vapor deposition (CVD) growth depends on the interplay among several experimental parameters due to the structural metastability of $MoTe_2$.[21] Both 1T' and 2H-$MoTe_2$ nanosheets can be synthesized by finely tuning the thermodynamics and kinetics of the $MoTe_2$ crystal growth during the experimental stage.[22] In addition, the low thermostability of $MoTe_2$ makes it decompose easily at high growth temperatures.[20] Furthermore, the balance between strain emergence and release during the tellurization reaction is also claimed to interpret $MoTe_2$ phase evolution. Therefore, exploring the full potential of this emerging material requires a reliable synthesis approach to selectively control its phase structure and uniform large-area growth. Till date, one of the big challenges is to synthesize large area $MoTe_2$ nanosheets with single phase. Among the few attempts Park et al. reported on synthesized cm^2 scale 1T' and 2H-$MoTe_2$ films via reversible phase transition engineering, where the phase transition is explained as driven by the mechanical strain and relaxation caused by the variable Te content.[23] Yang et al. obtained pure or mixed 1T' and 2H $MoTe_2$ by a fine control of Te velocity and reactor temperature on sapphire substrates.[24] More recently, Hynek et al. obtained large scale 2H-$MoTe_2$ by tellurization starting from the fine control of the initial thickness of pre-deposited MoO_3 thin film by atomic layer deposition on sapphire substrates.[25] Out of the flat case, Li et al. could achieve scalable CVD growth of high quality vertically aligned $MoTe_2$ with dominant 2H and 1T' phase, on Mo foils, by tuning growth time, temperature and geometry in the reactor process.[26] However, this target is hurdled by a still limited understanding of the tellurium chemisorption mechanism that seriously hampers large-area uniformity and phase selection.

In the present study, we performed a set of experiments to grow $MoTe_2$ by CVD as a function of the Te concentration gradient and the substrate orientation, in flat or tilt angle configurations, while keeping the other process parameters fixed, with the aim to sort out phase selectivity and obtain uniform, single phase $MoTe_2$ over large areas. To gain a deeper insight into this aspect, a phase transition mechanism from the metallic 1T' phase to the semiconducting 2H phase in $MoTe_2$ nanosheets is studied by guiding the experimental growth schemes with simulations based on finite element method (FEM).[27] First, we demonstrate a simple and reproducible way of large-area uniform growth of $MoTe_2$ up to 4 cm × 1 cm through detailed tellurization kinetics on the reaction surface using CVD. Here, we investigated the two geometrical configurations, namely flat and tilted orientations of the pre-deposited Mo film. Later, we show how to selectively tune the phase from 1T'-$MoTe_2$ to 2H-$MoTe_2$ by controlling the tellurium flow lines that drive Te concentration gradient, and by changing the geometrical settings, that is, the substrate tilt angle (20° and 45°) inside the

CVD reactor. To confirm the phase, quality, and uniformity, the as-grown $MoTe_2$ nanosheets were characterized by means of micro-Raman spectroscopy and atomic force microscopy (AFM).

2. Results and Discussions

2.1. Flat Mo Film

We employed an ambient pressure chemical vapor deposition (AP-CVD) apparatus to investigate the critical growth parameters for synthesizing $MoTe_2$ nanosheets. **Figure 1**a shows the schematic of the experimental set-up, consisting essentially of dual furnace CVD reactor, along with the substrate positioning inside a 2″ quartz tube. An e-beam evaporated Mo film on SiO_2(50 nm)/Si of 4 cm × 1 cm is placed at the bottom of the semi-cylindrical quartz crucible 2 facing upward in the direction parallel to the Te vapor flow from crucible 1. The same experimental conditions are adopted in FEM simulations developed with the COMSOL software (details in Experimental section and Supporting Information), to predict the Te concentration distribution in the reaction chamber and its spatial gradient. The calculations show that the Te concentration is homogeneous in the region of the substrate, Figure S1, Supporting Information. On the contrary, stark differences are predicted in the spatial distribution of the out-of-plane component of the Te gradient concentration, $\overline{V}C$, along the substrate surface, as graphed in Figure 1b by arrows, where intense vectors in red indicate a higher out-of-plane concentration gradient while blue arrows show lower out-of-plane concentration gradient (the corresponding in-plane component is illustrated in Figure S4a, Supporting Information).

To match the experimental results with the FEM simulations, dedicated experiments were conducted in the same configuration and growth parameters inside the CVD reactor. Micro-Raman spectroscopy investigations were performed on the as-grown $MoTe_2$ layers. Figure 1c shows the Raman spectra collected at different positions along the sample surface (dots in the optical picture). As evident from Raman spectra, $MoTe_2$ peaks are visible only in some positions, corresponding to grey dots in Figure 1c (inset), while in the positions marked with red dots no growth is detected. Characteristic Raman peaks are placed at 110 and 162 cm^{-1} corresponding to the out-of-plane A_u and B_g modes, respectively, and at 127 cm^{-1} corresponding to the in-plane E_{1g} mode of the 1T' $MoTe_2$ phase. The red arrow in Figure 1c inset indicates the flow direction of Ar carrier gas in the AP-CVD reactor. From Raman spectra it is clear that the 1T'-$MoTe_2$ region is present only at the front and edge parts of the sample surface. On the contrary, the spectra taken from the middle and downstream regions of the sample only display a peak at 300 cm^{-1} which is attributed to the second-order Raman mode of Si, from the substrate. On this basis, we can affirm that in the geometry configuration where the Mo film substrate is positioned as flat, only a minimal $MoTe_2$ growth is feasible at the upstream edge regions of the substrate and with a lack of lateral uniformity. To support this picture, we plot a distribution map considering the Raman intensity values of 1T'-$MoTe_2$ B_g phonon mode as a function of growth coverage

**ADVANCED
SCIENCE NEWS**

www.advancedsciencenews.com

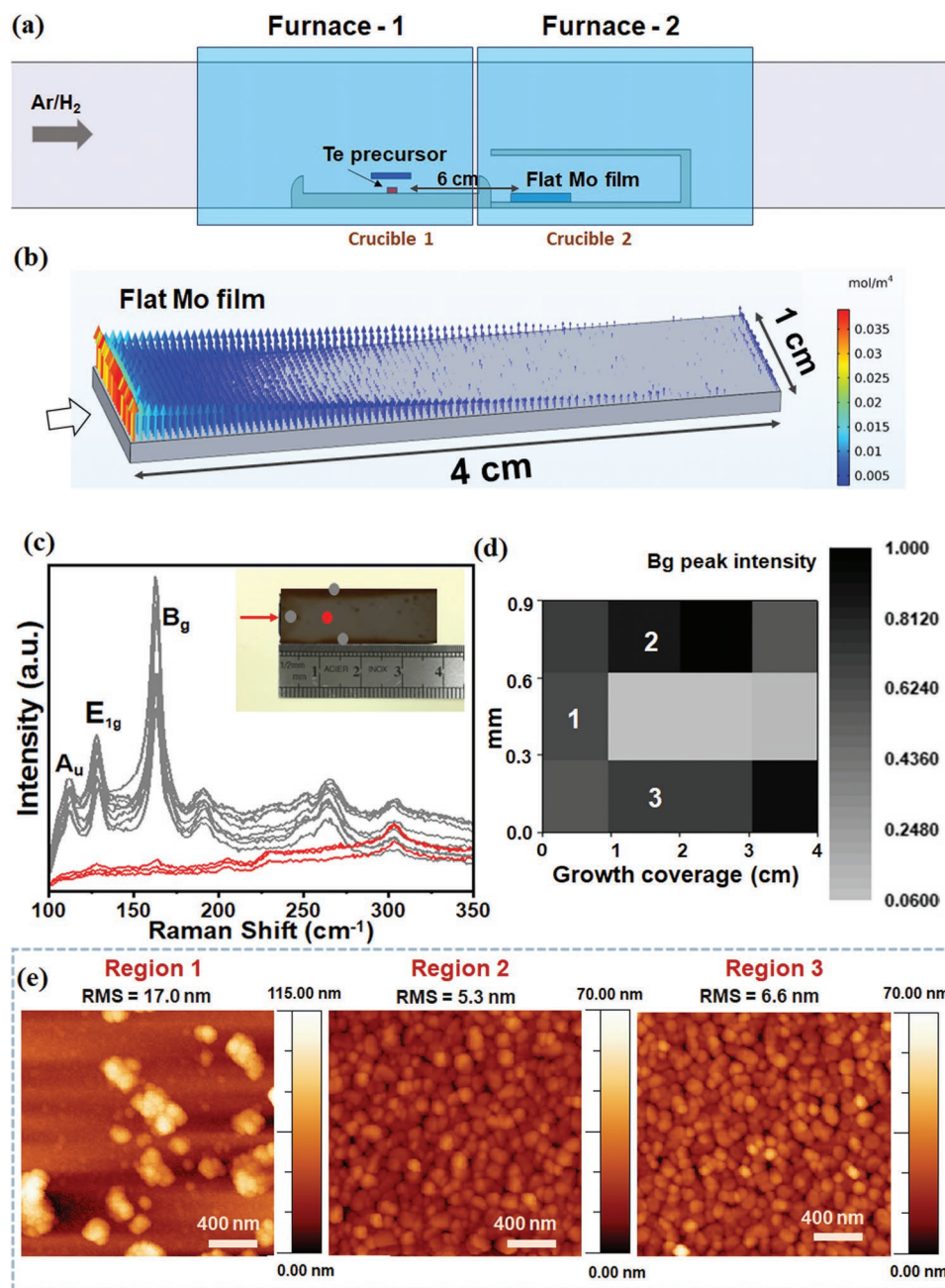**ADVANCED
MATERIALS
INTERFACES**

www.advmatinterfaces.de

Figure 1. a) CVD schematic illustration of the experimental set-up for $MoTe_2$ growth in flat configuration. b) View of the out-of plane component of Te concentration gradient distribution along 4 cm × 1 cm substrate size from COMSOL simulations. c) Raman spectra of as-grown $MoTe_2$ taken at different regions across the sample surface as indicated by the grey ($MoTe_2$ growth regions) and red (no growth) dots in the inset (flow direction indicated by red arrow). d) Raman map of Bg (g in pedix format) mode intensity distribution over 4 cm × 1 cm substrate size. e) AFM topography images of as-grown $MoTe_2$ taken at corresponding three regions 1, 2, and 3 in panel (d).

area as shown in Figure 1d. The map clearly shows that crystalline $MoTe_2$ growth (dark grey areas) with slight variations is found at the upstream and lateral edge regions while on the contrary, almost no growth takes place in the central region (light grey areas). Notably, the simulated spatial distribution of $\overline{V}C$ qualitatively reproduces the experimental results in locating the distribution of $MoTe_2$ growth over the substrate surface. To check the surface topography of the as-grown $MoTe_2$ AFM measurements were conducted in three different regions (1,

2, and 3 in Figure 1d). Considering the AFM image on the left in Figure 1e, corresponding to the region 1 of the sample, near the Te source, large grains with high root mean square (RMS) roughness value of 17.0 nm are visible. In particular, the formation of clusters is clearly inspected. Differently, in region 2 (Figure 1f middle) and region 3 (Figure 1f right), the AFM topographies show a compact and uniform deposition with RMS roughness of 5.3 (middle) and 6.6 nm (right). Further, according to AFM imaging, the average grain size

**ADVANCED
SCIENCE NEWS**
www.advancedsciencenews.com

**ADVANCED
MATERIALS
INTERFACES**
www.advmatinterfaces.de

in the regions 1, 2, and 3 is 279, 89, and 90 nm, respectively (detailed information in Figure S5a, Supporting Information). We speculate that the relatively high surface roughness at the upstream edge region of the substrate is a consequence of the high Te out-of-plane concentration gradient, as calculated from the simulations. In fact, by recalling Figure 1b, it is evident that the length of the (orange/yellow) arrows is maximized and confined at such edge of the sample. Thus, a significant reduction of the concentration gradient along the Mo film surface in the upstream to downstream direction of the gas flow (from left to right in Figure 1b,c inset) results in lower growth coverage. The findings from the simulations together with the experimental observations are essential for understanding the thermodynamics involved in the CVD-based MoTe$_2$ growth. As a consequence, we vary the CVD geometry in order improve the growth scalability and eventually obtain an extended continuous film.

2.2. Tilted Mo Film

We modified the geometrical configuration of the growth process by changing the orientation of the substrate inside the CVD reactor, in particular the position of the Mo film substrate at an arbitrary tilt angle (20°) inside the boat, facing toward the Te source. The aim is to investigate any possible variation in ∇C along the Mo film surface. **Figure 2**a shows the experimental schematic of CVD set-up, where a tilted Mo film sized 4 cm × 1 cm is placed at the bottom of the semi-cylindrical quartz crucible 2, tilted at 20° angle. The corresponding 3D simulation of ∇C for the given geometry is shown in Figure 2b. Precisely, the intensity and thermal scale represent the out-of-plane component of ∇C, where long red arrows stay for large ∇C while short blue arrows indicate small ∇C (the corresponding in-plane component is illustrated in Figure S4b, Supporting Information). Comparing these results with those for the flat case (Figure 1b), one can note that ∇C is here more uniformly distributed over the sample surface. Moreover, the modules of the ∇C vectors are order of magnitudes higher in the tilted case than the flat case, as can be noted by comparing the scale bar in Figures 1b and 2b. In the tilted case, ∇C is relatively high in the upstream edge region of the substrate, due to its vicinity to the Te vapor source and to the significant carrier gas velocity at the entrance of the crucible. Nonetheless, moving toward the substrate surface in the flow direction and thus reaching middle and the downstream edge, the Te concentration gradient shows almost homogeneous distribution, thus creating a favorable condition for the effective reaction with Mo and the growth of MoTe$_2$ over an extended area. We consider that such condition is due to the more uniform gas velocity profile caused by the reduction of the turbulent flow moving away from the crucible entrance (Figure S3, Supporting Information). It is worth noting that the arrows representing the Te concentration gradient are denser on the upstream side of the Mo film compared to the flat case, which indicates a major difference in the distribution of Te concentration gradient between the two configurations. Different distributions take place because, by tilting the substrate, the area facing the gas flow is larger than in the flat configuration, since the cross section facing toward the impinging flow is proportional to the incident angle of the flow and, consequently, the orientation angle of the substrate. Hence, the flux circulation becomes more intense in the tilted configuration and thus facilitates the Te chemisorption to the exposed Mo atoms on the substrate surface. On the contrary, in the flat substrate configuration, the directly exposed substrate area to the flow is limited to the upstream edge, which causes a lower Te concentration gradient in the downstream edge. This outcome can be understood in terms of the formation of the boundary layer at the interface between the flow and substrate.[28] Precisely, the boundary layer is the thin layer in the immediate vicinity of a bounding surface formed by the fluid flowing along the surface. In our case, we consider the boundary layer consisting of the Te vapor in (super)saturated condition floating on top of the Mo film substrate. When a boundary layer with a non-uniform (i.e., flow-dependent) thickness forms, the diffusion of the active gaseous species plays a significant role in the resulting growth quality. In our case, the tilting of the substrate surface can enhance the uniformity and reduce the thickness of such boundary layer compared to the flat case, thus inducing higher mass transport efficiency (h_g) across the substrate surface. Analytically, the mass transport efficiency follows the law $h_g = D_g/\delta$, where D_g is the gas diffusion coefficient and δ is the thickness of the boundary layer,[29] implying that a reduction in the thickness of the boundary layer improves the mass transport efficiency. Further, according to the Blasius model, $\delta \propto \sqrt{\dfrac{x}{U}}$, where x is the downstream distance from the start of the boundary layer, corresponding to the upstream edge of the sample in our case, and U is the free stream velocity.[30] From the simulation outcomes, in our geometric configurations the flow velocity decreases across the substrate surface, thus δ increases and h_g reduces moving in the flux direction progressively to the downstream edge of the substrate. Therefore, the observed difference in the velocity profile of the flow across the substrate will lead to the reduction of the nucleation density and lowers the MoTe$_2$ growth while moving in the gas flow direction across the substrate surface.

The sample after the MoTe$_2$ growth is shown in the photograph in Figure 2a, where large area coverage is directly visible. In the same image, the dots indicate the positions where Raman spectra were taken, to retrieve precise understanding of the layer quality and uniformity. The color code of each dot corresponds to the Raman spectrum plotted in Figure 2c, where the spectra were normalized to the intensity of the B_g peak and vertically shifted for the sake of clarity. We clearly identify the Raman spectrum corresponding to 1T'-MoTe$_2$ which exhibits the typical four main phonon modes: A_u at 108 and A_g 257 cm^{-1} associated to out-of-plane phonon modes plus E_{1g} at 127 and B_g at 163 cm^{-1} associated to in-plane phonon modes.[31] Identical Raman modes were observed in all the acquired regions over the substrate, confirming the uniformity in the thickness and the quality of the 1T'-MoTe$_2$ nanosheets growth. Figure 2d shows the normalized intensities (left y-axis, blue) of three main phonon modes A_u, E_{1g}, and B_g of the 1T'-MoTe$_2$ averaged over the different positions; the small error bar evidences the low degree of dispersion in the peak intensity, claiming for marginal changes in the different measured positions, and confirming the overall uniformity of MoTe$_2$ growth. Furthermore,
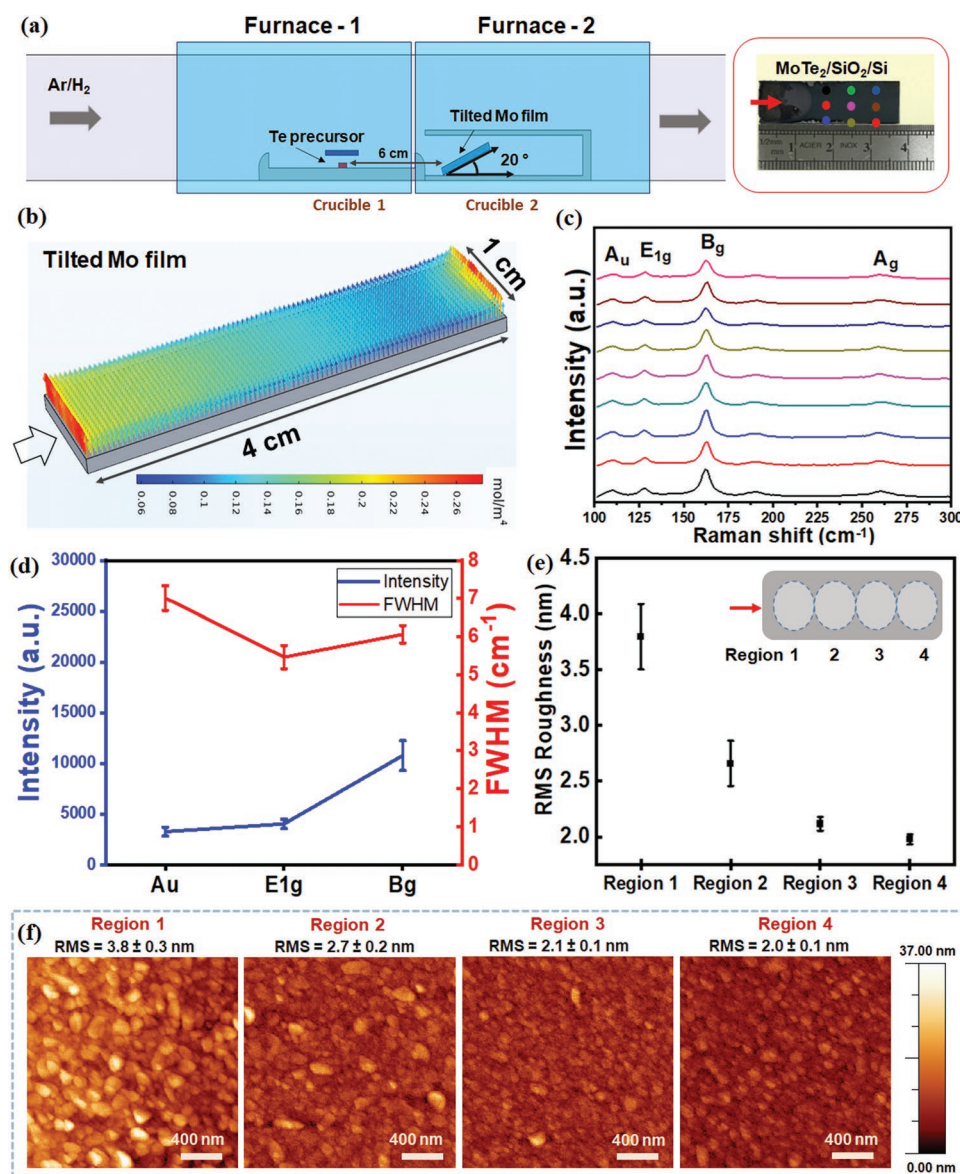
**ADVANCED
SCIENCE NEWS**

www.advancedsciencenews.com

**ADVANCED
MATERIALS
INTERFACES**

www.advmatinterfaces.de

Figure 2. a) CVD schematic illustration of the experimental set-up for MoTe$_2$ growth in tilted (20°) configuration and photograph of the obtained MoTe$_2$. b) COMSOL 3D model showing the Te concentration gradient along the 4 cm × 1 cm sample surface; the arrow indicates the flow direction. c) Raman spectra of 1T'-MoTe$_2$, normalized with respect to B$_g$ peak intensity, taken at different regions as indicated by the colored dots in the photograph in (a). d) Average (among the measured points) Raman intensity (blue y-axis) and FWHM (red y-axis) of 1T'-MoTe$_2$ A$_u$, E$_{1g}$, and B$_g$ phonon modes. e) RMS roughness from AFM collected at the different regions imaged in (f); the schematic in the inset identifies the different regions over the sample surface. f) AFM topography images of as-grown MoTe$_2$ taken at corresponding regions shown in (e) inset.

in Figure 2d, the full width half-maximum (FWHM, right y-axis, red) of the A$_u$, E$_{1g}$, and B$_g$ phonon modes, as extrapolated from the Voigt fitting, exhibits no apparent broadening with an error of less than 1 cm^{-1}, demonstrating that as-grown 1T'-MoTe$_2$ is highly crystalline.

The magnitude and distribution of out of plane component of the Te concentration gradient from FEM simulations is vectorially illustrated in Figure 2b, in a thermal scale where red/blue denotes high/low values. The magnitude decreases along the substrate surface in the gas flow direction, in line with the orientation and the spatial homogeneity of the as-grown MoTe$_2$ derived by AFM and Raman analysis, respectively. FEM simulations

indicate that the Te large concentration gradient standing toward the substrate at the upstream edge region closer to the Te precursor source can induce the formation of vertical nanostructures with high density confined in this region. In analogy with the pure CVD approach, where the out-of-plane precursor concentration gradient has a role in promoting the vertical growth of TMDs due to the Mullins–Sekerka mechanism,[27] moving from this edge inside the sample surface, the morphology evolves into a more continuous and uniform layer, consistently with the observed smaller variations and intensities of the simulated ∇C vectors. AFM investigations corroborate this model picture. The sample at the upstream edge region shows a morphology with

**ADVANCED
SCIENCE NEWS**
www.advancedsciencenews.com

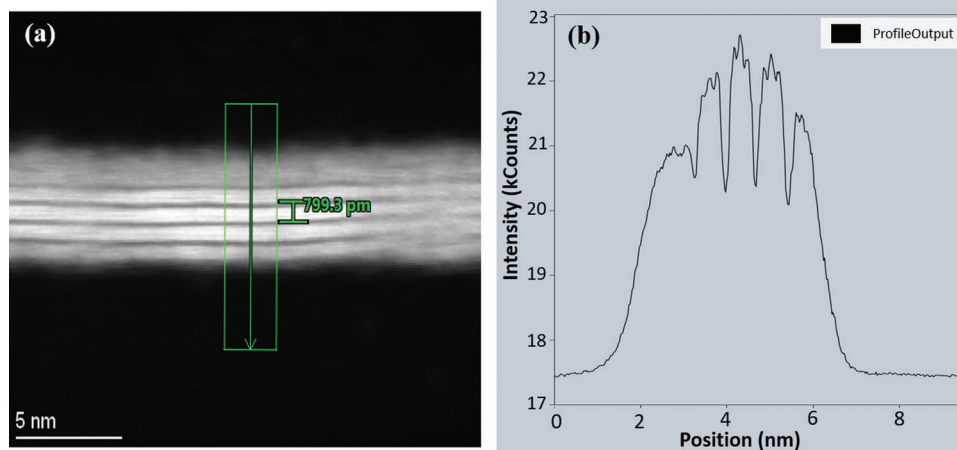**ADVANCED
MATERIALS
INTERFACES**
www.advmatinterfaces.de

Figure 3. a) HR-TEM HAADF cross section of a representative MoTe$_2$ nanosheet; single layers are evident and separated by van der Waals spacing; b) line profile across the MoTe$_2$ thickness, where the position of Mo and Te atoms can be elucidated.

protruding vertical domains with a relatively high RMS roughness of 3.8 ± 0.3 nm. Moving downstream, the sample surface evolves into a more uniform and smooth morphology with a progressive reduction in the roughness, which reaches a value as low as 2.0 ± 0.1 nm at the downstream edge region as shown in the graph in Figure 2e. Such values are extracted from the analysis of the AFM topographic images shown in Figure 2f, for the different regions located on the sample surface as in the sketch in the inset of Figure 2e. In addition, from AFM data, the average grain size in the regions 1–4 is 123 nm, 106, 83, and 66 nm, respectively (for a more detailed analysis, see Figure S5b, Supporting Information) Further analysis on the areal distribution of the grain size is included in Section S3, Supporting Information. Interestingly, we observe a linearly decreasing trend in the grain size from region 1 to region 4 with minimal roughness comparing to the flat case.

High-resolution transmission electron microscopy (HR-TEM) provided more insights into the structure of the nanosheets. **Figure 3**a shows high-angle annular dark field (HAADF) of a representative sample, obtained from the tellurization of a 8 nm pre-deposited Mo film (see AFM topographies in Section S5, Supporting Information), where the layered structure of each MoTe$_2$ sheets is clearly visible as a bright line 0.8 nm width. Each line is well separated by a dark region related to the interplanar van der Waals spacing. Considering in detail the cross section in Figure 3a, and focusing on the green box in the figure, from bottom to top it is possible to clearly recognize four layers, well aligned on the substrate surface. Moving to the surface the remaining layers appear defocused and possibly partially deteriorated; we attribute this finding to partial oxidation when the sample surface is exposed to the environment. Because of the Z number of Mo and Te atoms, it is not trivial to immediately distinguish them from the HR-TEM cross section, where a bright line accounts for the overall MoTe$_2$. However, considering the line profile taken across the thickness in the direction of the plotted green arrow, as shown in Figure 3b, is possible to distinguish a change in the intensity within each layer. Considering for instance the layer in the middle, a modulation consisting of two relative maxima aside of a main peak

is revealed. Such profile shape is associated with the position of each Mo and Te atom to form the MoTe$_2$ in the single layer.

2.3. Phase Tuning Strategy

Having clarified the key role of Te concentration gradient on the MoTe$_2$ growth and its dependence on the tilting of the substrate Mo film, a detailed study on their role in different geometrical configurations, would open a strategy for phase control in MoTe$_2$.

Figure 4a–c shows the FEM simulations results obtained when modeling three experimental conditions in the CVD reactor, namely for Te amount of 100 mg with 20° tilt angle for Mo film supporting substrate, 200 mg Te with 20° tilt angle, and 200 mg Te with 45° tilt angle. Considering Figure 4, FEM results are shown for the three cases. Specifically, in Figure 4a, we report the results already discussed in the previous sub-section with a tilt angle of 20° and 100 mg of Te, for a direct comparison with the results obtained in the other cases. As described above, in this case the FEM results are compatible with a uniform deposition of 1T' MoTe$_2$ all over the substrate surface.

The Raman spectra in Figure 4d obtained at three positions on the sample (upstream edge, middle and downstream edge, as imaged in the inset) show the presence of phonon modes at 108, 127, 257, and 163 cm^{-1} that can be assigned to the A_u, E_{1g}, and A_g out-of-plane and B_g in-plane vibrational modes of 1T' MoTe$_2$ phase, respectively.[31] The obtained Raman spectra, with their characteristic Raman peaks, confirm the formation of pure 1T' phase MoTe$_2$ over the 4 cm × 1 cm large area. Keeping the same configuration, in particular the substrate tilt angle at 20°, we repeated the experiment increasing the amount of Te to 200 mg, to study the influence of Te flux concentration. FEM in Figure 4b shows similar results as in Figure 4a. Incidentally, from FEM, we note that also the Te flow velocity at the substrate surface remains unchanged, while an evident increase in the Te concentration at the substrate surface with respect to the previous experiment is revealed. Thus, we should in principle expect no major changes in the grown
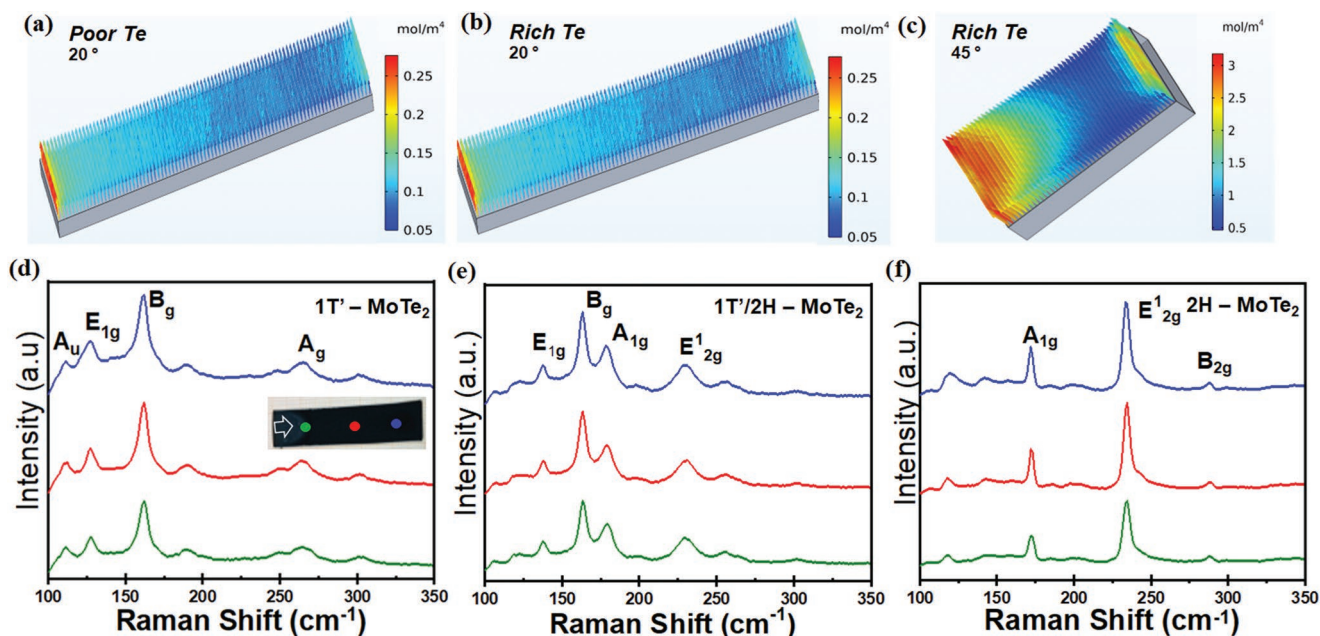
Figure 4. Effect of Te precursor amount and substrate tilt angle. FEM out-of-plane Te concentration gradient distribution on the sample surface: a) 100 mg Te and 20°; b) 200 mg Te and 20°; c) 200 mg Te and 45°. d–f) Raman spectra of pure MoTe$_2$ film obtained with conditions as in (a–c); note the identification of pure 1T' phase in (d), mixed 1T'/2H phase in (e), and pure 2H phase in (f). Regions of the sample where Raman measurements have been collected are shown in the inset of panel (d).

MoTe$_2$ film. However, when we consider the Raman spectra in Figure 4e, we detect peaks at 127 and 163 cm^{-1} that are assigned to the E_{1g} and B_g vibrational modes of the 1T' MoTe$_2$ phase and two other peaks at 172 and 232 cm^{-1} that can be assigned to the A_{1g} and E^1_{2g} vibrational modes of the 2H MoTe$_2$ phase. The measured Raman fingerprints reveal that increasing Te amount up to 200 mg (i.e., by 100% with respect to the previous case) and maintaining the tilt angle at 20° a mixed phase of 1T'/ 2H-MoTe$_2$ is obtained. This is mainly due to the increase of Te amount along the surface of the substrate, an observation that stresses the role of the precursor amount in the gas flow, when it reaches the substrate surface, in dictating the phase of the obtained MoTe$_2$, as also previously reported.[6]

For a clear understanding of the influence of Te concentration, Te gradient concentration and tilt angle, we performed an additional experiment where we increased the substrate tilt angle to 45° while keeping the Te precursor amount at 200 mg in the CVD reactor. Interestingly, FEM simulations revealed a modification in the distribution of the out of plane component of Te concentration gradient, as shown in Figure 4c. In particular, the average intensity of the out of plane component of Te concentration gradient, accompanied by a densification of the arrows, is higher with respect to the case of the lower tilt angle. This behavior can be simply explained in terms of a physical barrier to the carrier gas flow transporting the Te vapors. The higher tilt provokes a shadowing effect to the Te vapor. As a result of such a constraint Te tends to accumulate at the substrate surface until a dynamic equilibrium is reached, ultimately affecting the gradient distribution profile over the substrate surface with respect to the case of a lower tilt angle. The consequence has dramatic impact on the growth of MoTe$_2$, as evidenced in the Raman spectra shown in Figure 4f. Inter-

estingly, the analysis of the Raman spectra reveals the presence of peaks at 232 and 291 cm^{-1} that are associated with the E^1_{2g} and B_{2g} in-plane phonon modes plus a peak at 172 cm^{-1} associated with the A_{1g} out-of-plane phonon mode, all stemming from the 2H MoTe$_2$ phase, consistent with the typical Raman features reported for mechanically exfoliated flakes of the same allotropic phase.[32,33] The above findings indicate that the amount of Te in the reactor and the change in tilt angle, that is, the modification of the Te concentration gradient at the Mo containing substrate surface, allow us selectively to control the phase of the CVD grown MoTe$_2$ by tellurization approach from a pure 1T' to a pure 2H phase, passing through an intermediate configuration where mixed 1T'-2H are co-existing. Finally, it is noteworthy to observe that, in all the explored tilted configurations, in any case a continuous MoTe$_2$ thin film is achieved, developing uniformly over the macroscopic area of the substrate.

3. Conclusions

In this study, we successfully demonstrated the growth of crystalline MoTe$_2$ thin films in pure 1T', mixed 1T'/2H and pure 2H phase by tuning the configuration parameters in an atmospheric pressure CVD based on the tellurization of a predeposited Mo film on a SiO$_2$/Si substrate. On this scope, we performed finite elements simulations to predict the growth configurations of interest and correlate them with the experimental results on MoTe$_2$ film grown at the same conditions. We were able to synthesize uniform and continuous films over large areas up to 4 cm × 1 cm, limited by the size of the substrate to be accommodated in the tube furnace. Our synergistic

results from simulations and experiments reveal that, together with Te amount, the substrate tilt in the growth process dramatically defines the concentration gradient of the Te vapor at the reaction site thereby enabling us to achieve a close control of the MoTe$_2$ coverage over macro-scaled areas with a phase selective control, in a phase by design scheme. In extension, our work elucidates a method that could be considered as an efficient, scalable, and relatively simple solution to enable the controlled growth and optimize the characteristics of TMDs over large areas, whenever a chalcogenization CVD-based process is considered.

4. Experimental Section

MoTe$_2$ Sample Preparation and Growth: MoTe$_2$ was synthesized starting from molybdenum (Mo) films, pre-deposited by e-beam evaporation from Mo foil (99.9% Sigma-Aldrich, Darmstadt, Germany) on 50 nm SiO$_2$/Si substrates, in a two-temperature zone furnace CVD apparatus, using a tellurization approach. To this scope, in the CVD reactor, tellurium powder (100 mg; 99.997%, Sigma-Aldrich, Darmstadt, Germany) were placed in a ceramic boat in the center of the upstream furnace and the Mo supporting substrate was placed face-up in a fully closed boat at the starting corner of the downstream furnace, respectively. The distance between the Te source and the Mo containing boat was kept fixed at 6 cm. The orientation of the Mo containing substrate inside the closed quartz boat changed in the various experiments from flat (Figure 1a) and tilted (Figure 2a) geometrical configurations. An Ar/4%H$_2$ flow was used as carrier gas to favor the transport of the Te vapor from the upstream furnace, where it forms, toward the downstream furnace, where the heterogeneous vapor-solid reaction with Mo takes place to form MoTe$_2$ nanosheets at suitable temperature. The carrier gas flow and temperature profiles used in the AP-CVD process are shown in Figure S8, Supporting Information, where the blue line and right y-axis refers to Ar/H$_2$ flux, while the temperature profile is shown by the black line for the upstream (Te) furnace and red line for the downstream (Mo) furnace. In detail, temperature controllably ramps from RT up to 600 °C in the first 25 min, followed by a plateau, where the MoTe$_2$ growth is maintained for 60 min at 625 and 650 °C for downstream (Mo) and upstream (Te) furnaces, respectively. Afterward, the temperature profile followed the natural system cooling down to room temperature.

MoTe$_2$ Sample Characterization: MoTe$_2$ samples were characterized using Raman spectroscopy and AFM. Confocal Raman spectroscopy was performed using a spectrometer (Renishaw InVia) equipped with a solid-state laser source of excitation wavelength 514 nm (2.41 eV) in backscattering configuration. The laser radiation was focused on the sample by means of a 50 × Leica objective (0.75 numerical aperture), maintaining the incident laser power less than 1 mW to avoid any sample damage. AFM (Bruker, Dimension edge) in tapping mode with ultrasharp silicon probes was used to collect 2 μm × 2 μm surface topography maps of the grown MoTe$_2$ and retrieve rms roughness employing WSxM software. For the HR-TEM images, the lamellae were investigated by means of Scanning TEM (STEM) techniques. The images were performed with a Thermo-Fischer Themis Z G3 aberration-corrected transmission electron microscope equipped with an electron gun monochromator operating at 200 kV acceleration voltage.

Finite Element Simulations: The simulation of the flow dynamics in the CVD reactor was conducted with the finite element method (FEM) implemented in the software package COMSOL Multiphysics. A model was implemented to estimate the velocity streamlines of the carrier gas, the Te precursor concentration and concentration gradient, at the different regions inside the reaction chamber, focusing in particular in the region where the Mo containing substrate is located. This model was based on coupled Navier–Stokes and mass diffusion equations solved simultaneously within the FEM scheme. In details, the gas flow rate (ρ),

in the laminar flow regime, was determined by solving the Navier-Stokes Equation (1):

$$\rho\left(\frac{\partial u}{\partial t} + u\nabla u\right) = -\nabla p + \nabla\left(\mu\left(\nabla u + (\nabla u)^T\right) - \frac{2}{3}\mu(\nabla u)I\right) + F; \frac{\partial\rho}{\partial t} + \nabla(\rho u) = 0 \tag{1}$$

where u is the velocity field, p the pressure, μ the dynamic viscosity, I the unit matrix, and F is the volumetric applied force (i.e., gravity); the superscript T indicates the transposed matrix. Concomitantly, the transport of diluted species, accounting for the flow assisted diffusion of Te precursor, was obtained by solving the following mass diffusion Equation (2):

$$R = \frac{\partial c}{\partial t} + \nabla(-D\nabla c) + u\nabla c; N = -D\nabla c + u \tag{2}$$

where R is the source term of the precursor, c the precursor concentration, D the diffusion coefficient, and N the precursor flux. The real geometrical constrains, in terms of boat dimension, distance and positioning of Te precursor and substrate were treated in the FEM by defining a free tetrahedral mesh of the domains consisting of 844 004 mesh elements plus 2 410 699 internal degrees of freedom for a total of 958 872 discretization domains. To ensure mesh independent results, the mesh was refined creating several small-sized elements in the area adjacent to the substrate domain. Further technical details of FEM simulations, including detailed graphs and schematics can be found in Supporting Information.

Statistical Analysis: The AFM topographies consisted of a matrix of 256 rows × 256 columns. The data of each AFM matrix were analyzed by means of WSxM software for plane correction and root-mean-square (rms) roughness defined as

$$\text{rms} = \sqrt{\frac{\sum_{i,j}\left(a_{ij} - a\right)^2}{N}} \tag{3}$$

where a_{ij} is the matrix data point at row i and column j, a the mean value, and N the number of points (i.e., $N = 256 \times 256 = 65.536$ points). The error bars of the rms roughness value were calculated by using the standard deviations of the roughness value with respect to the mean value calculated over several images acquired in the same spatial region of the sample.

For the Raman spectra, peak fitting was obtained by using commercial software Wire, from Renishaw. The peaks were fitted with pseudo-Voigt functions.

Statistics on the AFM and Raman data were also conducted by using the software Origin Pro.

Supporting Information

Supporting Information is available from the Wiley Online Library or from the author.

Conflict of Interest

The authors declare no conflict of interest.

Data Availability Statement

The data that support the findings of this study are available from the corresponding author upon reasonable request.

Keywords

[1] M. Chhowalla, Z. Liu, H. Zhang, *Chem. Soc. Rev.* **2015**, *44*, 2584.

[2] S. Manzeli, D. Ovchinnikov, D. Pasquier, O. v. Yazyev, A. Kis, *Nat. Rev. Mater.* **2017**, *2*, 17033.

[3] W. Choi, N. Choudhary, G. H. Han, J. Park, D. Akinwande, Y. H. Lee, *Mater. Today* **2017**, *20*, 116.

[4] X. Xu, X. Li, K. Liu, J. Li, Q. Feng, L. Zhou, F. Cui, X. Liang, Z. Lei, Z. Liu, H. Xu, *Cryst. Grow. Des.* **2018**, *18*, 2844.

[5] S. Cho, S. Kim, J. H. Kim, J. Zhao, J. Seok, D. H. Keum, J. Baik, D.-H. Choe, K. J. Chang, K. Suenaga, S. W. Kim, Y. H. Lee, H. Yang, *Science* **2015**, *349*, 625.

[6] C. Martella, A. Quadrelli, P. P. Tummala, C. Lenardi, R. Mantovan, A. Lamperti, A. Molle, *Cryst. Growth Des.* **2021**, *21*, 2970.

[7] Z. Wang, D. Gresch, A. A. Soluyanov, W. Xie, S. Kushwaha, X. Dai, M. Troyer, R. J. Cava, B. A. Bernevig, *Phys. Rev. Lett.* **2016**, *117*, 056805.

[8] T. Zhang, L. Fu, *Chem* **2018**, *4*, 671.

[9] M. Bhatnagar, M. Gardella, M. C. Giordano, D. Chowdhury, C. Mennucci, A. Mazzanti, G. della Valle, C. Martella, P. Tummala, A. Lamperti, A. Molle, F. Buatier de Mongeot, *ACS Appl. Mater. Interfaces* **2021**, *13*, 13508.

[10] J.-H. Li, D. Bing, Z.-T. Wu, G.-Q. Wu, J. Bai, R.-X. Du, Z.-Q. Qi, *Chin. Phys. B* **2020**, *29*, 017802.

[11] R. Zazpe, H. Sopha, J. Charvot, R. Krumpolec, J. Rodriguez-Pereira, J. Michalička, J. Mistrík, D. Bača, M. Motola, F. Bureš, J. M. Macak, *Appl. Mater. Today* **2021**, *23*, 101017.

[12] A. V. Kolobov, P. Fons, J. Tominaga, *Phys. Rev. B* **2016**, *94*, 094114.

[13] F. Zhang, H. Zhang, S. Krylyuk, C. A. Milligan, Y. Zhu, D. Y. Zemlyanov, L. A. Bendersky, B. P. Burton, A. V. Davydov, J. Appenzeller, *Nat. Mater.* **2019**, *18*, 55.

[14] L. Sun, M. Ding, J. Li, L. Yang, X. Lou, Z. Xie, W. Zhang, H. Chang, *Appl. Surf. Sci.* **2019**, *496*, 143687.

[15] M. Yamamoto, S. T. Wang, M. Ni, Y.-F. Lin, S.-L. Li, S. Aikawa, W.-B. Jian, K. Ueno, K. Wakabayashi, K. Tsukagoshi, *ACS Nano* **2014**, *8*, 3895.

[16] Y.-F. Lin, Y. Xu, S.-T. Wang, S.-L. Li, M. Yamamoto, A. Aparecido-Ferreira, W. Li, H. Sun, S. Nakaharai, W.-B. Jian, K. Ueno, K. Tsukagoshi, *Adv. Mater.* **2014**, *26*, 3263.

[17] S. Fathipour, N. Ma, W. S. Hwang, V. Protasenko, S. Vishwanath, H. G. Xing, H. Xu, D. Jena, J. Appenzeller, A. Seabaugh, *Appl. Phys. Lett.* **2014**, *105*, 192101.

[18] F. Tumino, C. Grazianetti, C. Martella, M. Ruggeri, V. Russo, A. L.i Bassi, A. Molle, C. S. Casari, *J. Phys. Chem. C* **2021**, *125*, 9479.

[19] G. Z. Magda, J. Pető, G. Dobrik, C. Hwang, L. P. Biró, L. Tapasztó, *Sci. Rep.* **2015**, *5*, 14714.

[20] L. Sun, M. Ding, J. Li, L. Yang, X. Lou, Z. Xie, W. Zhang, H. Chang, *IOP Conf. Ser.: Mater. Sci. Eng.* **2019**, *677*, 022123.

[21] M. S. Sokolikova, C. Mattevi, *Chem. Soc. Rev.* **2020**, *49*, 3952.

[22] S. Yang, X. Xu, W. Xu, B. Han, Z. Ding, P. Gu, P. Gao, Y. Ye, *ACS Appl. Nano Mater.* **2020**, *3*, 10411.

[23] J. C. Park, S. J. Yun, H. Kim, J.-H. Park, S. H. Chae, S.-J. An, J.-G. Kim, S. M. Kim, K. K. Kim, Y. H. Lee, *ACS Nano* **2015**, *9*, 6548.

[24] L. Yang, W. Zhang, J. Li, S. Cheng, Z. Xie, H. Chang, *ACS Nano* **2017**, *11*, 1964.

[25] D. J. Hynek, R. M. Singhania, S. Xu, B. Davis, L. Wang, M. Yarali, J. V. Pondick, J. M. Woods, N. C. Strandwitz, J. J. Cha, *ACS Nano* **2021**, *15*, 410.

[26] J. Lin, H. Wang, R. Y. Taj, H. Li, M. Shakerzadeh, S. H. Tsang, Z. Liu, E. H. T. Teo, *Nano Res.* **2020**, *13*, 2371.

[27] K. Momeni, Y. Ji, K. Zhang, J. A. Robinson, L.-Q. Chen, *npj 2D Mater. Appl.* **2018**, *2*, 27.

[28] T. B. Limbu, B. Adhikari, S. K. Song, B. Chitara, Y. Tang, G. N. Parsons, F. Yan, *RSC Adv.* **2021**, *11*, 38839.

[29] H. Rubin, J. Atkinson, *Environmental Fluid Mechanics*, CRC Press, Boca Raton, London **2001**.

[30] C. Miao, C. Zheng, O. Liang, Y.-H. Xie, in *Physics and Applications of Graphene – Experiments*, (Ed: S. Mikhailov), IntechOpen, London **2011**, Ch. 3.

[31] T. A. Empante, Y. Zhou, V. Klee, A. E. Nguyen, I.-H. Lu, M. D. Valentin, S. A. Naghibi Alvillar, E. Preciado, A. J. Berges, C. S. Merida, M. Gomez, S. Bobek, M. Isarraraz, E. J. Reed, L. Bartels, *ACS Nano* **2017**, *11*, 900.

[32] Q. Wang, J. Chen, Y. Zhang, L. Hu, R. Liu, C. Cong, Z.-J. Qiu, *Nanomaterials* **2019**, *9*, 756.

[33] C. Ruppert, O. B. Aslan, T. F. Heinz, *Nano Lett.* **2014**, *14*, 6231.